Astronomy & Astrophysics manuscript no. qubicanddustdecorrelation
September 7, 2023

Identifying frequency decorrelated dust residuals in B-mode maps by exploiting the spectral capability of bolometric interferometry

M. Regnier[1], E. Manzan[2,3], J-Ch. Hamilton[1], A. Mennella[2,3], J. Errard[1], L. Zapelli[2,3], S.A. Torchinsky[1,4], S. Paradiso[5,6], E. Battistelli[8], P. De Bernardis[8], L. Colombo[2], M. De Petris[8], G. D'Alessandro[8], B. Garcia[11], M. Gervasi[10], S. Masi[8], L. Mousset[7], N. Miron Granese[13,14,15], C. O'Sullivan[9], M. Piat[1], E. Rasztocky[12], G.E Romero[12], C.G. Scoccola[13,14], and M. Zannoni[10]

[1] Université Paris Cité, CNRS, Astroparticule et Cosmologie, F-75013 Paris, France
[2] Università degli studi di Milano, Italy
[3] INFN sezione di Milano, 20133 Milano, Italy
[4] Université PSL, Observatoire de Paris, AstroParticule et Cosmologie, F-75013 Paris, France
[5] Waterloo Centre for Astrophysics, University of Waterloo, Waterloo, ON N2L 3G1, Canada
[6] Department of Physics and Astronomy, University of Waterloo, Waterloo, ON N2L 3G1, Canada
[7] Institut de Recherche en Astrophysique et Planetologie, Toulouse (CNRS-INSU), France
[8] Universita di Roma - La Sapienza, Italy
[9] National University of Ireland, Maynooth, Ireland
[10] Università di Milano – Bicocca and INFN Milano-Bicocca
[11] ITeDA-Mza.(CNEA, CONICET, UNSAM)
[12] Instituto Argentino de Radioastronomía (CCT La Plata, CONICET; CICPBA; UNLP), Buenos Aires, Argentina
[13] Consejo Nacional de Investigaciones Científicas y Técnicas (CONICET), Godoy Cruz 2290, Ciudad de Buenos Aires C1425FQB, Argentina
[14] Facultad de Ciencias Astronómicas y Geofísicas, Universidad Nacional de La Plata, Paseo del Bosque, La Plata B1900FWA, Buenos Aires, Argentina
[15] Universidad de Buenos Aires, Facultad de Ciencias Exactas y Naturales, Departamento de Física, Intendente Güiraldes 2160, Ciudad Universitaria, Ciudad de Buenos Aires C1428EGA, Argentina

Received September 15, 1896; accepted March 16, 2197

ABSTRACT

Context. Astrophysical polarized foregrounds represent the most critical challenge in Cosmic Microwave Background (CMB) B-mode experiments. Multi-frequency observations can be used to constrain astrophysical foregrounds to isolate the CMB contribution. However, recent observations indicate that foreground emission may be more complex than anticipated. Not properly accounting for these complexities during component separation can lead to a bias on the recovered tensor-to-scalar ratio.
Aims. In this paper we investigate how the increased spectral resolution provided by band splitting in Bolometric Interferometry (BI) through a technique called *spectral imaging* can help control the foreground contamination in the case of unaccounted Galactic dust frequency decorrelation along the line-of-sight (LOS).
Methods. We focus on the next generation ground-based CMB experiment CMB-S4, and compare its anticipated sensitivities, frequency and sky coverage with a hypothetical version of the same experiment based on bolometric interferometry (CMB-S4/BI). We perform a Monte-Carlo analysis based on parametric component separation methods (FGBuster and Commander) and compute the likelihood on the recovered tensor-to-scalar ratio, r.
Results. The main result of this analysis is that spectral imaging allows us to detect systematic uncertainties on r from frequency decorrelation when this effect is not accounted for in component separation. Conversely, an imager like CMB-S4 would detect a biased value of r and would be unable to spot the presence of a systematic effect. We find a similar result in the reconstruction of the dust spectral index, where we show that with BI we can measure more precisely the dust spectral index also when frequency decorrelation is present and not accounted for in component separation.
Conclusions. The in-band frequency resolution provided by BI allows us to identify dust LOS frequency decorrelation residuals where an imager of similar performance would fail. This opens the prospect to exploit this potential in the context of future CMB polarization experiments that will be challenged by complex foregrounds in their quest for B-modes detection.

Key words. cosmic microwave background – inflation – ISM – data analysis

1. Introduction

This paper addresses one of the burning questions currently concerning the CMB community: are there reliable strategies to validate or invalidate a detection of primordial B-modes in the presence of complex, polarized, Galactic foregrounds ? The scope of our paper is not to provide a comprehensive answer to this problem, but to investigate a possible solution that exploits the spectral imaging capability of an unconventional technique for CMB polarimetry, called bolometric interferometry (BI) applied to controlling interstellar dust foreground emissions residuals.

Indeed, the next generation of satellites like Litebird (Hazumi et al. 2019) and PICO (Hanany et al. 2019) and ground-

based experiments like Simons Observatory (Ade et al. 2019) and CMB-S4 (Abazajian et al. 2022) aim at improving the constraint on the tensor-to-scalar ratio, r, at the level of 0.001 and below. Accurate foregrounds (and systematic effects) removal is already the main limiting factor.

To improve foreground removal, modern experiments are relying on multi-frequency observations and on improved models of astrophysical emissions. For example, there are many PySM[1] (Thorne et al. 2017) models that have been developed with the goal of simulating the effects of deviations from the single modified blackbody (MBB) emission conventionally assumed for the Galactic dust thermal emission. The models **d5** and **d7** take into account different dust grain compositions (Hensley & Draine 2017), while the models **d4** and **d12** describe the dust emission as a sum of two or up to six single MBBs along each line-of-sight (LOS) (Finkbeiner et al. 1999; Martínez-Solaeche et al. 2018).

This article focuses on the **d6** model which introduces frequency decorrelation along each line of sight by making Gaussian realizations of a deviation from the MBB emission at each frequency following the correlation matrix derived by Vansyngel et al. (2018).

Frequency decorrelation of the dust emission arises from spatial variation of the dust spectral energy distribution (SED) over the sky as well as along the LOS due to the underlying structure of the Galactic magnetic field. This effect is usually quantified at the power spectra level by means of the correlation ratio, R_ℓ (Planck Collaboration et al. 2017). The most recent observational evidence regarding this effect comes from Planck Collaboration et al. (2017, 2020); Pelgrims et al. (2021); Ritacco et al. (2023) and could affect polarimetric and spectral calibration in the case of wide beam instruments (Masi et al. 2021) as well as cause bias on the tensor-to-scalar ratio (McBride et al. 2023; Hensley & Bull 2018).

If dust indeed does not behave as a simple MBB (as it is usually assumed) but exhibits more complex spectral features, like frequency decorrelation, we need some method to detect the presence of foreground residuals in our results. This could be achieved by comparing results from different sky patches, as proposed by Aurlien et al. (2022), or by cross-checking with different component separation methods, such as parametric ones (Eriksen et al. 2006; Stompor et al. 2008), blind one (Aumont & Macías-Pérez 2007) or the moment expansion (Chluba et al. 2017; Vacher et al. 2022), some of which might be less sensitive to foreground mismodelling.

Another possibility, which we illustrate in this paper, is to use BI and its ability to discriminate frequencies in-band during data analysis. This allows us to achieve a spectral resolution of a few GHz[2] and reanalyze the same data with different spectral configurations. A variation in the constraint on r from one configuration to another is a hint of a contamination at the level of the tensor-to-scalar ratio due to component separation residuals.

In this paper we investigate the advantage of BI for foreground removal and characterization by comparing the performance in detecting dust frequency decorrelation of one of the most advanced experiments to come, CMB-S4, with a similar, hypothetical experiment based on bolometric interferometry, that we name CMB-S4/BI. We carry out the study with simulations based on two different component separation codes: FGBuster (Stompor et al. 2008) and Commander (Eriksen et al. 2006, 2008). In the main body of this paper we focus on FGBuster simulations, while we report the study with Commander in Appendix B. Because we propose a new methodology, we neglected the impact of instrumental systematic effects in our study.

The paper is organized as follows. In Sect. 2 we provide a brief introduction to bolometric interferometry and to its state-of-the-art, represented by the QUBIC experiment (Hamilton et al. 2022, and references therein). Sect. 3.1 is dedicated to the description of the simulated sky models, instrumental configurations and the Monte-Carlo pipeline based on the FGBuster (Stompor et al. 2008) component separation code. Here we also describe a machine learning classification used to assess the ability to detect residuals from foreground emissions in a single realization. In Sect. 3.2 we compare the results in terms of tensor-to-scalar ratio reconstruction from simulations with conventional foreground models and with unaccounted Galactic dust frequency decorrelation. We also discuss the performance of the machine learning classification algorithm in terms of its ability to detect r measurements contaminated by residual dust emission. In Appendix A we present the results obtained with FGBuster regarding the estimation of foreground parameters while in Appendix B we discuss all the results obtained with Commander.

2. Bolometric interferometry and QUBIC in a nutshell

In this section we briefly describe the principles of BI, focusing on a specific feature of this technique, called *spectral imaging*, which is at the base of our study. We also provide the reader with an overview of the QUBIC experiment, currently the only experiment based on BI. The interested reader can find more details on BI, QUBIC and *spectral imaging* in Hamilton et al. (2022); Mousset et al. (2022); Torchinsky et al. (2022) while the instrument is described in Piat et al. (2022); Masi et al. (2022); D'Alessandro et al. (2022); Cavaliere et al. (2022); O'Sullivan et al. (2022).

2.1. Principles of bolometric interferometry

Bolometric interferometry is a technique that combines the use of bolometers, which are state-of-the-art wide-band cryogenic detectors providing high sensitivity, with the advantages in terms of systematic effects control provided by interferometry through the *self-calibration* technique, commonly used in radio-interferometry (Cornwell & Wilkinson 1981). The application to BI is detailed in Bigot-Sazy et al. (2013).

Figure 1 shows a schematic of the QUBIC instrument, highlighting the fundamentals of BI. The sky signal enters the cryostat through an aperture window and is transmitted to a series of filters, a step-rotating half-wave plate, a polarizing grid and an array of paired back-to-back feed-horn antennas. The back horns directly illuminate an optical combiner, which focuses the radiation onto two focal planes through a dichroic plate.

When the instrument observes a distant point source along the optical axis an interference pattern forms on the two focal planes. The left panel of Fig. 2 shows a simulation of this pattern. As a result, each focal plane element measures the sky through a specific beam pattern called the *synthesized beam* shown in the right panel of Fig. 2 as well as inFig. 4. The instrument observes the sky signal convolved by the synthesized beam. The construc-

[1] `https://pysm3.readthedocs.io/en/latest/`

[2] Some level of in-band frequency sensitivity is actually achievable to traditional imagers by using the small variations in the spectral properties of different detectors. This was successfully applied to map the CO emission line (Planck Collaboration et al. 2014).

tive or destructive interference of the incoming signal defines a series of peaks and nulls, with properties that depend on the signal wavelength, λ, on the number of horns along the maximum axis of the antenna array, P, and on the separation between two consecutive horns, Δh, as follows (Mousset et al. 2022):

$$\theta_{\rm FWHM} = \frac{\lambda}{(P-1)\Delta h}, \quad \Theta = \frac{\lambda}{\Delta h}, \tag{1}$$

where $\theta_{\rm FWHM}$ is the half power width of the peaks and Θ is the angular distance between the main peak and the first secondary peaks.

Equation 1 shows, in particular, that the position of the secondary peaks is particularly sensitive to λ. As an example, in the right panel of Fig. 2 we show a cut of the synthesized beam at a fixed azimuthal angle for two frequencies: 140 GHz and 160 GHz.

Knowing how the multiple-peaked shape of the synthesized beam evolves with frequency allows us to recover the sky signal during data analysis at different frequencies within the physical band. This is possible as long as two frequencies, ν_1 and ν_2, are far enough that the secondary peaks are well-resolved, therefore if $\Theta(\nu_2) - \Theta(\nu_1) > \theta_{\rm FWHM}(\sqrt{\nu_1\nu_2})$, which occurs for $\frac{\Delta\nu}{\nu} \geq \frac{1}{P-1}$. We call this technique *spectral imaging*.

The dependence of secondary peaks on frequency allows us to achieve a spectral resolution of a few GHz within the physical band. Furthermore, because spectral imaging happens at the data analysis level, it allows us to re-analyze the same data with different spectral configurations, which can help us detect biases in our results. This is an unique asset compared to traditional imagers, that would need several focal planes coupled to multichroic filters to achieve the same spectral performance. A Fourier-transform spectrometer would suffer from a noise penalty related to not observing all frequencies simultaneously.

In this context, our aim is to investigate how the increased spectral resolution provided by BI can help in controlling the contamination from Galactic foregrounds and constrain foreground complexity in the quest for primordial B-modes detection, with a special focus on the Galactic dust emission.

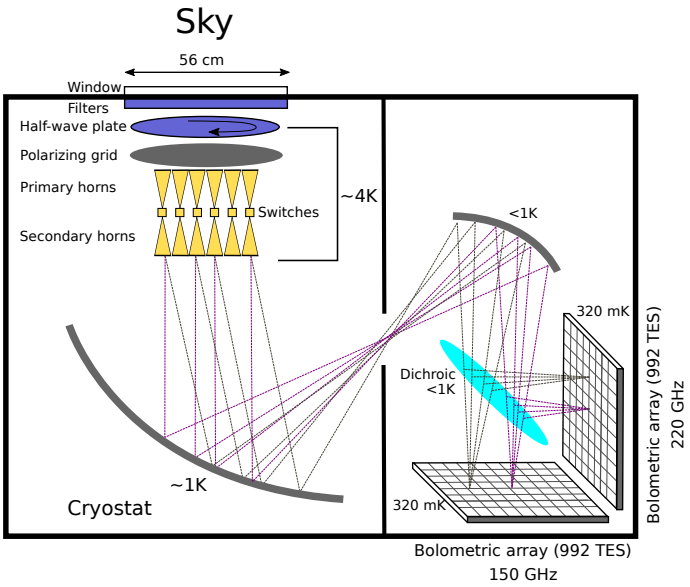

Fig. 1. Schematic of the QUBIC instrument showing the principle of bolometric interferometry. The sky signal is received by an array of back-to-back horns and re-imaged onto the bolometric focal planes where the field interferes additively. A polarizer and a rotating half-wave plate make the instrument sensitive to linear polarization.

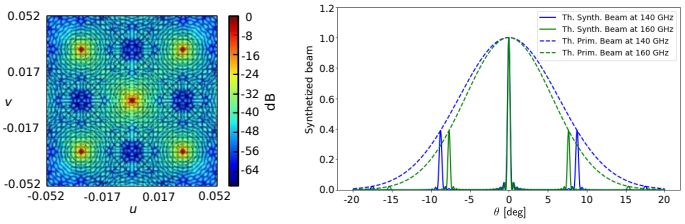

Fig. 2. *Left panel*: simulation of the interference pattern on the focal plane generated by a monochromatic point source. *Right panel*: azimuth cut of the *synthesized beam* (solid lines) at 140 GHz (blue line) and at 160 GHz (green line) for a detector at the center of the focal plane. Dashed lines represent the beam pattern of a single feed-horn. One can appreciate the frequency-dependent position of the secondary peaks.

2.2. The QUBIC instrument

QUBIC is the first CMB B-modes experiment based on bolometric interferometry. The instrument observes the sky in two frequency bands, centered at 150 GHz and 220 GHz, respectively, with a 25% bandwidth. Each feed-horn array is made by 400+400 back-to-back antennas and each focal plane is equipped with 992 TES bolometers. QUBIC will observe from the Alto Chorrillos site, in the Argentinian Andes, at about 5000 meters a.s.l. and will provide an upper limit on $r < 0.015$ at 68% C.L. after three years of observations (Hamilton et al. 2022).

The first QUBIC prototype is referred to as the *technological demonstrator* (TD), a reduced version of the instrument to demonstrate bolometric interferometry with laboratory measurements and sky observations. The QUBIC-TD uses the same cryostat (Masi et al. 2022), HWP (D'Alessandro et al. 2022) and polarizing grid as the final instrument, but will observe only in the 150 GHz channel. It is equipped with smaller diameter mirrors, a smaller feed-horn array made by 64+64 back-to-back feed-horns and a smaller focal plane, made by 248 bolometers.

After extensive laboratory testing the QUBIC-TD was installed at the observation site during November 2022 (see Fig. 3). Routine observations will start after commissioning. The interested reader can find the details of the laboratory tests and their results in: Hamilton et al. (2022); Mousset et al. (2022); Torchinsky et al. (2022); Piat et al. (2022); Masi et al. (2022); D'Alessandro et al. (2022); Cavaliere et al. (2022); O'Sullivan et al. (2022).

The top-left panel of figure 4 (taken from Hamilton et al. 2022) shows the synthesized beam measured by one of the focal plane TES detectors compared to a simulation of the same beam (top-right panel). The bottom panel of the same figure (taken from Torchinsky et al. 2022) shows the synthesized beams measured at various frequencies. These data show the multiple-peaked shape of the synthesized beam with good agreement with the theoretical predictions and the expected frequency dependence of the secondary peak positions. The measured instrumental noise (detectors and read-out) is 2.06×10^{-16} W/ $\sqrt{\rm Hz}$ (Piat et al. 2022) and the median cross-polarization of the detectors is 0.12% (D'Alessandro et al. 2022).

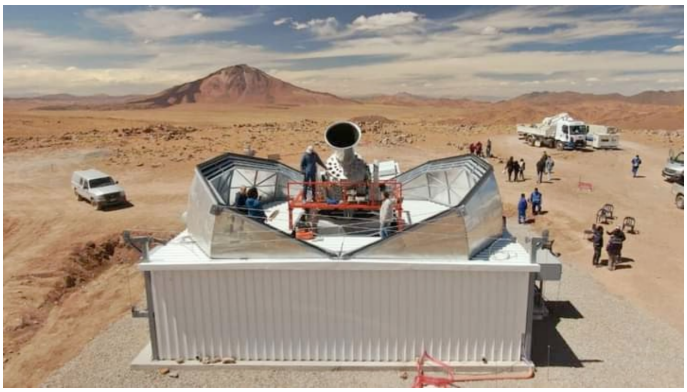

Fig. 3. QUBIC-TD in the Alto Chorrillos site. The cryostat is placed on a movable mount to scan in azimuth and elevation. The system is placed inside a motor-controlled dome that can be opened and closed.

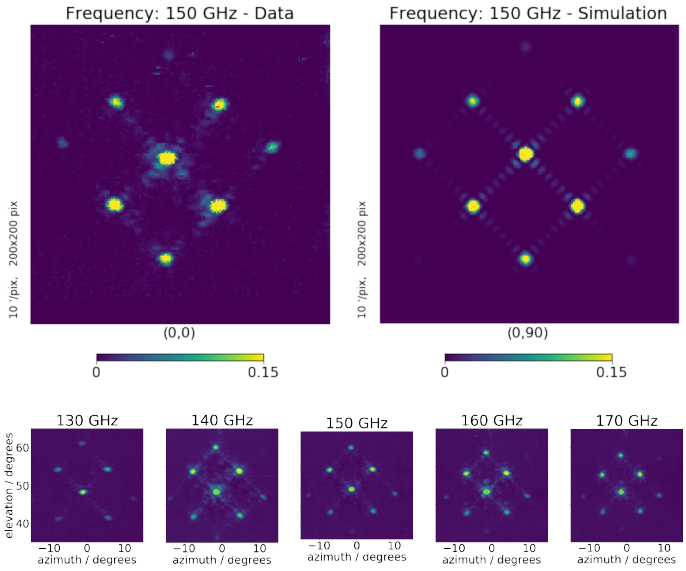

Fig. 4. *Top panel*: synthesized beam measured for one detector at 150 GHz (left) compared with the simulated 150 GHz synthesized beam for the same detector (right, from Hamilton et al. 2022). *Bottom panel*: synthesized beam for one detector measured at various frequencies (from Torchinsky et al. 2022).

3. Dust decorrelation with bolometric interferometry and direct imaging

This paper aims to quantify the effect of various dust models with increasing complexity on the component separation results and demonstrate the benefits of spectral imaging in this regard. We focus, in particular, on the LOS frequency decorrelation of thermal dust, a phenomenon already observed in Planck data (Pelgrims et al. 2021).

To quantify dust decorrelation, we follow Planck Collaboration et al. (2020), and use the quantity $\mathcal{R}_\ell$, defined in Eq. (2):

$$\mathcal{R}_\ell^{\nu_1\times\nu_2} = \frac{C_\ell^{\nu_1\times\nu_2}}{\sqrt{C_\ell^{\nu_1\times\nu_1}\times C_\ell^{\nu_2\times\nu_2}}}. \quad (2)$$

$\mathcal{R}_\ell$ is the ratio between the crossed spectrum between two frequencies ν_1 and ν_2 and the square root of the product of the auto-spectra at these same frequencies. This ratio is close to 1 for completely correlated thermal dust. In our sky simulations we can increase or decrease the level of complexity in the thermal dust spectral energy density (SED) by tuning $\mathcal{R}_\ell$ to a value farther or closer to one.

To assess the potential of BI, we compare the component separation performance of CMB-S4 to a BI version of the same experiment having the same sensitivity per unit bandwidth, but allowing for a higher spectral resolution through band-splitting thanks to spectral imaging. In the following subsections we present the methods used for this comparison.

3.1. Methods

3.1.1. Simulated sky

Our sky model contains the CMB plus synchrotron and dust emission foregrounds.

We simulated the CMB using angular power spectra provided by the `fgbuster` package that are based on the latest Planck 2018 results[3]. We used the following two FITS files:

(i) `Cls_Planck2018_lensed_scalar.fits` in which B modes are considered with $r = 0$ and lensing,
(ii) `Cls_Planck2018_unlensed_scalar_and_tensor_r1.fits` in which B modes are considered with $r = 1$ and no lensing.

In our simulations we used TT, EE and TE spectra taken directly from the file (i), while the BB spectrum was obtained by summing the BB spectrum from the file (i) multiplied by a lensing residual of 0.1 with the BB spectrum from the file (ii) multiplied by the considered value of r (either 0 or 0.006). Note that such a simplified approach, neglecting the additional tensor contribution to the TT, TE and EE spectra, is sufficient in our case as we only perform the likelihood analysis on the BB spectrum.

For the foregrounds we considered the following models[4]:

1. model **d0s0**, which assumes a single modified black-body (MBB) emission for the thermal dust and a power law emission for the synchrotron, with constant dust spectral index across the sky, $\beta_\mathrm{d} = 1.54$, dust temperature, $T_\mathrm{d} = 20\,\mathrm{K}$, and synchrotron spectral index, $\beta_\mathrm{s} = -3$, with no curvature.
2. model **d1s1**, derived from the Planck data post-processed with the Commander code (Planck Collaboration et al. 2016) for the dust component. Synchrotron emission is taken from Haslam emission at 408 MHz in Remazeilles et al. (2015), Haslam et al. (1982). The thermal dust is modeled as a modified black body with spatially varying temperature and spectral index, synchrotron is modeled as a power law with spatially varying spectral index with no curvature;
3. model **d6s1**. This model is derived from **d1s1** with the introduction of LOS frequency decorrelation in the dust emission following the approach described in Eq. (14) of Vansyngel et al. (2018). The correlation length, ℓ_corr, is a parameter defined by PySM to vary the degree of decorrelation: the smaller the decorrelation length, the larger the decorrelation.

Whereas models **d0s0** and **d1s1** are fixed realizations, model **d6s1** results in a random realization of the SED in which the dispersion is determined by the correlation length ℓ_corr. Figure 5

[3] Spectra can be accessed at `https://github.com/fgbuster/fgbuster/tree/master/fgbuster/templates`
[4] See `https://pysm3.readthedocs.io/en/latest/#models` for more details about the models.

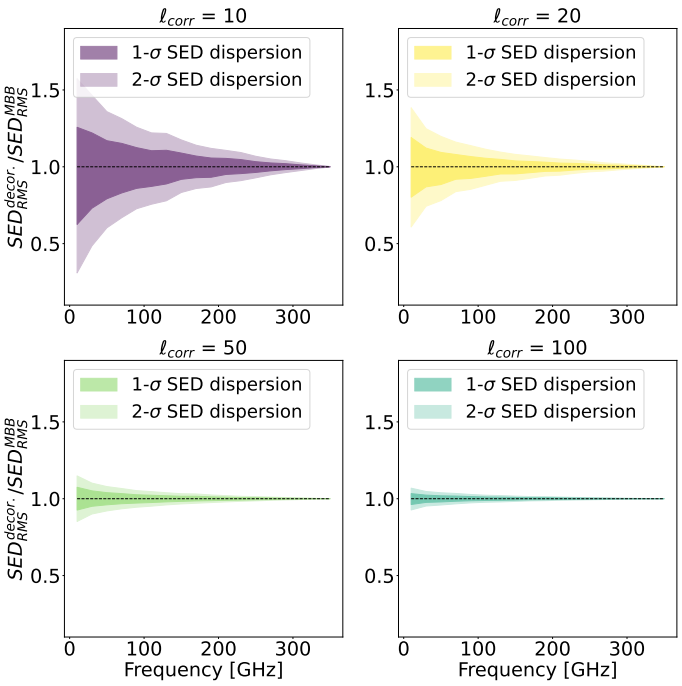

Fig. 5. Dispersion of the dust SED for different correlation lengths of the PySM **d6** model normalized by the single MBB emission (**d1** model). The colored areas represent the statistical deviation from a MBB for a given correlation length, evaluated over 500 realizations.

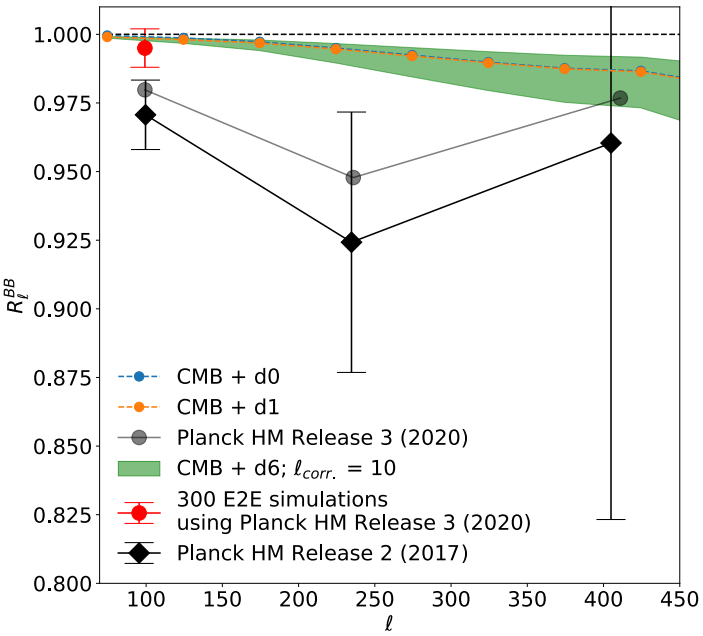

Fig. 6. Correlation ratio measured by Planck from the Half Mission (HM) maps at 217 GHz and 353 GHz, compared to the same ratio obtained from a simulation with the PySM CMB template plus the dust models **d0**, **d1** and various realizations of the **d6** with $\ell_{\rm corr} = 10$. Black points are from Fig. 2 of Planck Collaboration et al. (2017), gray points are from Fig. B.2 of Planck Collaboration et al. (2020), the red point has been obtained from the values in the middle plot of the second row in Fig. 18 of Planck Collaboration et al. (2020).

displays the dispersion of various SED realizations as a function of $\ell_{\rm corr}$, showing that the dispersion increases with a shorter correlation length.

We explore the effect of dust LOS frequency decorrelation with a level of decorrelation consistent with current observations. Specifically, the range of correlation lengths used in our study is $\ell_{\rm corr} \geq 10$, which corresponds to a decorrelation level below 5% for all the simulated frequencies. This configuration represents a conservative scenario with respect to the decorrelation level measured by Planck (Planck Collaboration et al. 2017, 2020) in the same multipole range considered in our work ($\ell \leq 300$ – see Fig. 6 for a comparison with Planck estimates).

3.1.2. Instrument models

The first instrument considered in our analysis is CMB-S4 (Abazajian et al. 2022), which will observe at 9 different frequencies in the 20–280 GHz range to constrain both synchrotron and thermal dust emissions. CMB-S4 goal will be the detection of r at the level $r > 0.003$ with more than 5σ.

The second instrument is a version of CMB-S4 based on bolometric interferometry (CMB-S4/BI), where each of the bolometer-based (i.e. above 85 GHz) physical frequency band, $\Delta\nu_i$, can be subdivided into $n_{\rm sub}$ sub-bands of width:

$$\Delta\nu_i^{\rm BI} = \frac{\Delta\nu_i}{n_{\rm sub}}. \quad (3)$$

If we now consider m frequency bands of CMB-S4, each one subdivided in $n_{\rm sub}$ sub-bands in CMB-S4/BI we can calculate the sensitivity in each sub-band as:

$$\sigma_{j,i}^{\rm BI} = \sigma_j \times \sqrt{n_{\rm sub}} \times \varepsilon, \quad (4)$$

where σ_j is the CMB-S4 sensitivity in the j-th sub-band within i-th physical band, $n_{\rm sub}$ is the number of sub-bands and ε is a term introduced to account for the sub-optimality of bolometric interferometry (for further details about BI sub-optimality see Mousset et al. 2022).

Two approximations have been done regarding the instrument models:

1. the noise is always considered to be white, although in CMB-S4/BI we have added the multiplicative term ε to account for the sub-optimality of bolometric interferometry. We know that the noise of a bolometric interferometer is not completely white and this calls for specific component separation techniques able to deal with correlated noise. These techniques are currently being developed within the QUBIC collaboration.
2. we have neglected the angular resolution of the optical beam to be consistent with the CMB-S4 reference paper. The physical beam affects the final sensitivity of both instruments but it should not impact the generality of our results.

Figure 7 shows the bandwidths and sensitivities of some among the tested experimental configurations. For each CMB-S4 frequency interval above 85 GHz we have studied seven configurations of CMB-S4/BI with $n_{\rm sub}$ ranging from 2 to 8. Increasing the number of sub-bands results in a sensitivity degradation according to equation (4) with ε between 20% and 60% taken from Mousset et al. (2022). Because we focus on dust decorrelation we have not subdivided the synchrotron frequency bands so that the first three intervals of the various configurations overlap. Note that because the simulated CMB-S4 sky patch is centered far away from the Galactic plane, we expect the correlations between dust and synchrotron to be negligible for the scope of our study.

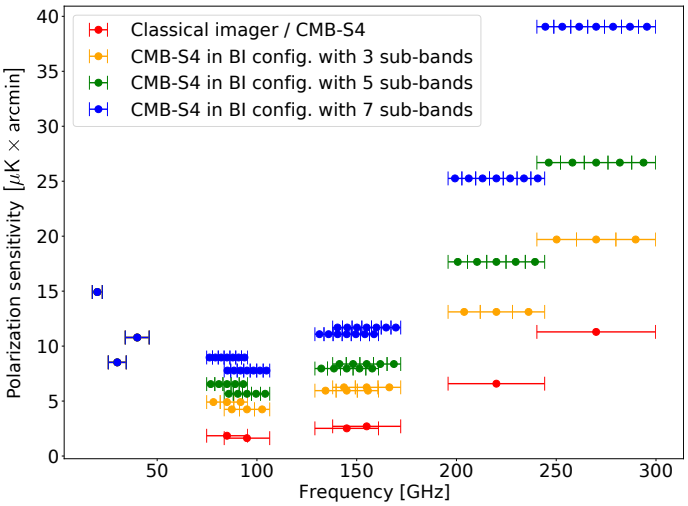

Fig. 7. Polarization sensitivity of CMB-S4 and three examples of CMB-S4/BI, with $n_{\rm sub} = 3, 5, 7$ respectively. Notice that the bands of the three lowest frequency channels are identical for all the instruments. Because our study focuses on dust decorrelation we have chosen not to split the bandwidths of the synchrotron channels.

We emphasize that because this band-splitting is performed at the data analysis level, one can explore various values of the number of sub-bands $n_{\rm sub}$ with the same dataset. Studying the evolution of the resulting constraints as a function of $n_{\rm sub}$ is the core of this study.

3.1.3. Simulation pipeline

We describe here the simulation pipeline for the Monte-Carlo analysis that we performed using the FGBuster parametric component separation code. In Appendix B.1 we report the same information regarding the simulations performed with Commander.

In the FGBuster analysis we considered the sky patch shown in Fig. 8, that corresponds to the currently expected patch that will be observed by CMB-S4.

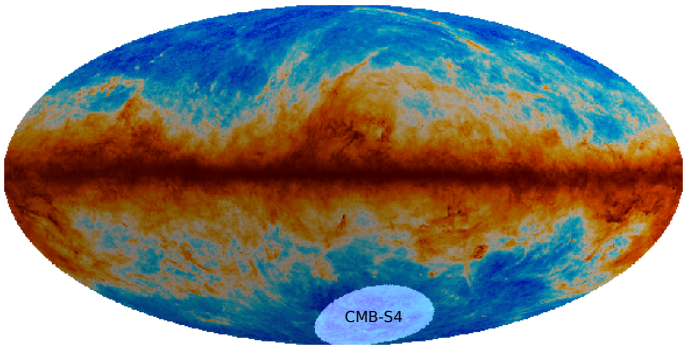

Fig. 8. The sky patch observed by CMB-S4, also used in our simulations. The patch (highlighted in white) is centered in a relatively clean sky area, as one can see from the dust map at 150 GHz plotted underneath.

We considered eight instrument configurations (see also Fig. 7): the CMB-S4 configuration (parametrized following (Abazajian et al. 2022)) and seven versions of CMB-S4/BI, obtained by dividing each frequency band. We then applied component separation and analyzed the cross-spectra of the resulting maps using a uniform binning (see Table 1 for a summary of the simulation set-up).

Table 1. Parameters used for analyzing simulations with FGBuster

Map $N_{\rm side}$	256
Multipole range	21–335
$\Delta\ell$	35
Input r	0, 0.006
Residual lensing fraction[1]	10%
Sky fraction [%]	3%
Sky patch center[2] [Equatorial coord.]	$\alpha = 0°$ $\beta = -45°$

[1]This is the fraction of the lensing signal left in the CMB map.
[2]Center of CMB-S4 sky patch.

For each instrument configuration, the overall analysis chain consisted in the following steps:

1. generate a CMB realization as described at the beginning of Sect. 3.1.1;
2. generate a noise realization for each frequency channel in the considered instrument configuration;
3. add the CMB and the noise to the foregrounds maps generated as described in Sect. 3.1.1.
4. apply component separation to the input maps. In some cases we assumed the same model used to generate the input case, in others we assumed a different model, to mimic a realistic situation in which the actual foregrounds are not 100% known and one might assume a model that does not completely describe reality.
5. perform a cross-spectra analysis between two noise realizations (each with half the exposure time) to recover the tensor-to-scalar ratio, r. We calculated angular power spectra using the NaMaster[5] code (Alonso et al. 2019) with an apodization radius of 4 deg.

In Table 2 we list the various cases studied in this work. Each case was simulated with all the instrument configurations described in Sect. 3.1.2 and Fig. 7.

Component Separation. We performed parametric component separation modelling our data as follows:

$$\boldsymbol{d}_p = \mathbf{A} \cdot \boldsymbol{s}_p + \boldsymbol{n}_p, \tag{5}$$

where p is the pixel index, $\boldsymbol{d}_p$ and $\boldsymbol{n}_p$ are vectors representing the data and noise measured by the instrument frequency channels, $\boldsymbol{s}_p$ is a vector containing the "true" sky values at the same frequencies, and $\mathbf{A}$ is a mixing matrix that contains information about the sky components (CMB, synchrotron and interstellar dust). In our simulations we considered the dust temperature as a known parameter, $T_{\rm d} = 20\,{\rm K}$. Thus, the only unknown parameters for synchrotron and dust emissions were their spectral indices, $\beta_{\rm s}$ and $\beta_{\rm d}$.

[5] https://namaster.readthedocs.io/en/latest/

Table 2. Cases analyzed in this work.

Input foreground model		Model assumed in component separation
d0s0		**d0s0**
d1s1		**d1s1**
d6s1	$\ell_{\rm corr} = 10$	**d1s1**
	$\ell_{\rm corr} = 13$	
	$\ell_{\rm corr} = 16$	
	$\ell_{\rm corr} = 19$	
	$\ell_{\rm corr} = 100$	

FGBuster solves for the best spectral indexes, $\beta_{\rm s}$ and $\beta_{\rm d}$, given the data, $\boldsymbol{d}_p$, and the noise covariance matrix, $\mathbf{N}$, following the spectral likelihood approach of Stompor et al. (2008). It is worth mentioning that to cope with computational constraints (processing time and computer memory) and keeping the same parameters as in Abazajian et al. (2022), in the case of **d1s1** and **d6s1** we reconstructed the spectral indices on maps with $N_{\rm side} = 8$, corresponding to a pixel resolution of about 7°.

Tensor-to-scalar ratio estimation. The main goal of our study is to asses how residuals caused by biased estimates of foreground parameters impact the reconstruction of the tensor-to-scalar ratio, r, which is the main parameter characterizing the primordial CMB B-modes. We write the likelihood on r using a Gaussian approximation:

$$-2\ln\mathcal{L}(r) = \left(\mathbf{D}^{BB}_{\ell,\rm exp} - \mathbf{D}^{BB}_{\ell,\rm model}\right)^T \mathbf{N}^{-1}_{\ell,\ell} \left(\mathbf{D}^{BB}_{\ell,\rm exp} - \mathbf{D}^{BB}_{\ell,\rm model}\right) \quad (6)$$

where $\mathbf{D}^{BB}_{\ell,\rm exp}$ and $\mathbf{D}^{BB}_{\ell,\rm model}$ are the measured and theoretical angular power spectra, $\mathbf{N}^{-1}_{\ell,\ell}$ is the inverse of the sum of the noise and sample variance covariance matrices, and $\ln\mathcal{L}(r)$ the likelihood on r.

In the cases where we used the **d6s1** model as the sky input we assumed a different and simpler model in the component separation, namely the **d1s1** model. This approach allowed us to evaluate a realistic situation in which the sky emissions are more complex than we think, and the use of a parametric model may result in a biased estimation of r. Therefore, in these cases we performed the log-likelihood evaluation using the noise covariance matrix in Eq. (6), $\mathbf{N}$, obtained from simulations without frequency decorrelation in the dust emission.

3.1.4. Detecting dust decorrelation on a single realization

We used machine learning to test the ability of BI to detect foreground residuals that may be present when the assumed foregrounds model is different from that describing the actual sky emissions. That might occur, for example, if one assumes a **d1s1** model when the sky is described by a **d6s1** model. We therefore explore the possibility to classify between *contaminated* and *not contaminated* cases that both end up producing the same average reconstructed r for an imager (described by the case in which we do not split the physical band in sub-bands).

This ability is a key issue when an experiment detects a tensor-to-scalar ratio that is significantly different from zero. In this case there is only one realization (i.e., the actual measurement) to understand whether there are unknown systematic effects biasing the value beyond the uncertainty set by the noise plus the known systematic effects.

We carried out this test by performing a machine learning classification based on a simple gradient boosted decision tree (a `GradientBoostingClassifier` from the `scikit-learn` Python library[6]) according to these steps:

1. produce 500 sky realizations with $r = 0.006$[7] in which the sky is generated with **d1s1** and fitted with the same model (we call this dataset **d1-d1**), this dataset is labelled as "clean";
2. produce 500 simulations with $r = 0$, in which the sky is generated with **d6s1** ($\ell_{\rm corr} = 10$) and fitted with **d1s1** (we call this dataset **d6-d1**), this dataset is labelled as "contaminated";
3. for each simulation and for each value of $n_{\rm sub}$ calculate the following two quantities: $\rho(n_{\rm sub}) = r(n_{\rm sub})/r(n_{\rm sub} = 1)$ and $\sigma_\rho(n_{\rm sub}) = \sigma(r(n_{\rm sub}))/\sigma(r(n_{\rm sub} = 1))$ ("training" dataset), both with "clean" or "contaminated" label, depending on the model used as an input. These quantities are those that discriminate whether we have foreground residuals or not: if $\rho \neq 1$ it means that the detection depends on the number of sub-bands and, therefore, is likely to be affected by foreground residuals;
4. train the network with 250 **(d1s1,** $r = 0.006$**)** and 250 **(d6s1,** $r = 0$**)** randomly selected realizations from the training dataset (using 100 cross-validation subsets);
5. calculate $\rho(n_{\rm sub})$ and $\sigma_\rho(n_{\rm sub})$ for the remaining 250 **(d1s1,** $r = 0.006$**)** and 250 **(d6s1,** $r = 0$**)** simulations ("test" dataset);
6. feed the trained network with the values calculated in step 5 to test its ability to classify the simulations as "clean" (constant $\rho(n_{\rm sub})$) or "contaminated" (variable $\rho(n_{\rm sub})$).

The result of this procedure is the so-called "confusion matrix", i.e., a matrix that compares the results from the classification predicted by the algorithm with the true one.

3.2. Results

3.2.1. Reconstruction of the tensor-to-scalar ratio, r

Here we discuss the results of our simulations in terms of the reconstruction of the tensor-to-scalar ratio, r. The performance in terms of foreground reconstruction is discussed in Appendix A (FGBuster simulations) and Appendix B.2 (Commander simulations).

The four panels in Fig. 9 show the histograms of the maximum likelihood estimates (normalized to the maximum and smoothed with a kernel density estimator, KDE) for the reconstruction of r as a function of $n_{\rm sub}$ in four different cases.

Top-left panel. Here we have the CMB with $r_{\rm input} = 0$ and **d0s0** foregrounds. In this case the reconstructed r does not depend on $n_{\rm sub}$ and there is a small bias due to an $E \rightarrow B$ modes leakage caused by the power spectra computation on a sky patch, where the spherical harmonics are no longer orthogonal. This bias could be mitigated by increasing the apodization radius of the mask at the expense of a smaller effective sky fraction

[6] https://scikit-learn.org/

[7] The value of $r = 0.006$ was chosen so that the average reconstructed r matched the bias that would be obtained from a map with CMB with $r = 0$ and **d6s1** foregrounds removed assuming a **d1s1** model with a single reconstructed sub-band(see Fig. 11)

(< 3%). This optimization, however, is outside the scope of the paper.

Top-right panel. Here we have the CMB with $r_{\rm input} = 0$ and **d1s1** foregrounds. Also in this case we see that the reconstructed r does not depend on $n_{\rm sub}$, even if the complexity of the dust emission is higher (the dust spectral index varies in the sky). However, here we observe a slightly larger bias in r with respect to the **d0s0** case, caused by the aforementioned leakage and also by the difference in pixel size of the reconstructed maps ($N_{\rm side} = 8$) compared to the input sky ($N_{\rm side} = 256$).

Bottom-left panel. Here we have the CMB with $r_{\rm input} = 0.006$ and **d1s1** foregrounds. This case is similar to the previous one, the only difference being the value of $r_{\rm input}$.

Bottom-right panel. Here we have the CMB with $r_{\rm input} = 0$ and **d6s1** foregrounds fitted with the **d1s1** model. The histograms show that fitting with a model that does not account for frequency decorrelation produces distributions that are larger for smaller values of $n_{\rm sub}$. Also the mean value of the reconstructed r obtained from such distributions varies, and becomes smaller as $n_{\rm sub}$ increases.

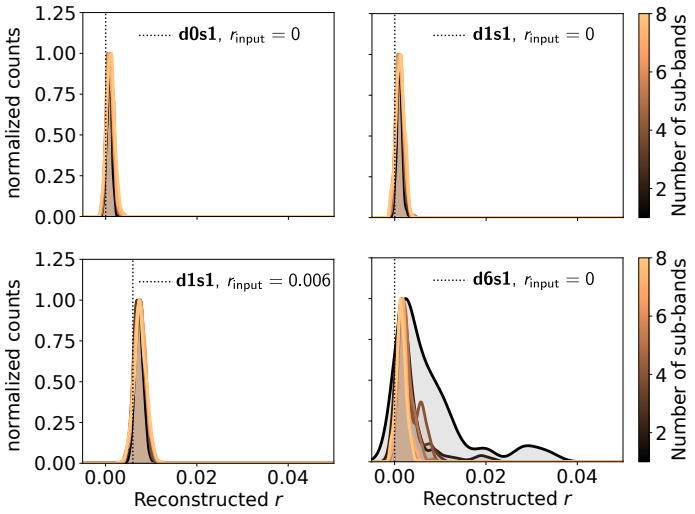

Fig. 9. Normalized histograms of the reconstructed r as a function of the number of sub-bands. *Top-left*: model **d0s0** with $r_{\rm input} = 0$. *Top-right*: model **d1s1** with $r_{\rm input} = 0$. *Bottom-left*: model **d1s1** with $r_{\rm input} = 0.006$. *Bottom-right*: model **d6s1** with $\ell_{\rm corr} = 10$ and $r_{\rm input} = 0.0$.

In Fig. 10, for each of the four cases we plot the recovered tensor-to-scalar ratio as a function of $n_{\rm sub}$.

The blue, orange and green curves refer to the case in which we fit for the same dust model used to simulate the input sky. In these three cases the recovered r does not depend on $n_{\rm sub}$, as one would expect for a detection not contaminated by foregrounds. The difference between the recovered r with respect to $r_{\rm input}$ that we see in all the three cases is caused by the $E \rightarrow B$ leakage and pixel size effects discussed above.

The red curve refers to the case in which the input sky contains dust emission with frequency decorrelation while component separation was performed ignoring this feature, assuming the **d1s1** model. In this case, the increase in the number of frequency maps provided by BI allows us to better constrain the spectral indices, thus reducing the bias as the number of sub-bands increases. A classical imager (represented by $n_{\rm sub} = 1$) would measure $r \sim 0.008$ while a bolometric interferometer would see this estimate reducing by increasing $n_{\rm sub}$. This would indicate that the first value of r is an artifact due to the presence of residual dust emission.

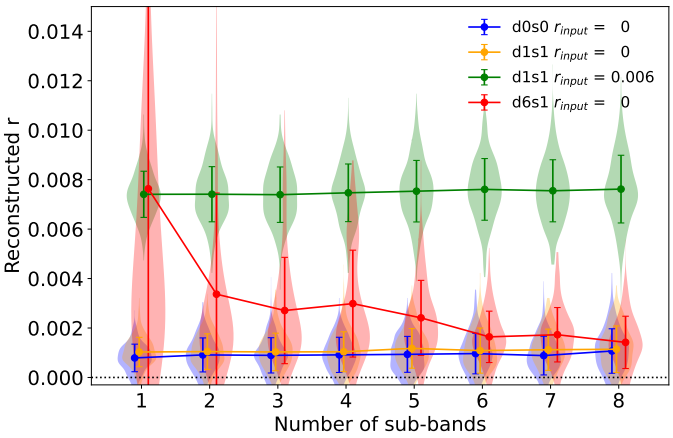

Fig. 10. Reconstructed r and standard-deviation as a function of the number of sub-bands in the case of unaccounted dust frequency decorrelation (model **d6s1** with $\ell_{\rm corr} = 10$ and $r = 0$) compared to two cases of no decorrelation (model **d1s1**): $r = 0$ and $r = 0.006$. On top of extracted r values and their standard deviation, we have overplotted the shape of the distribution as a "violin plot".

Figure 11 shows the mean and standard deviation of the reconstructed r for all the simulated dust models with $r_{\rm input} = 0$, including **d6s1** with various correlation lengths: $\ell_{\rm corr.} = 10, 13, 16, 19, 100$. For the sake of simplicity, we only show four instrument configurations: CMB-S4 and CMB-S4/BI with 3, 5, 7 sub-bands. As one can see, the advantage of BI in diagnosing foreground residuals and therefore decreasing the bias on r is maintained even in the case of smaller levels of dust frequency decorrelation. As expected, in the limit of $\ell_{\rm corr.} = 100$ the result is compatible with the case of a single modified black-body (model **d1s1**).

3.2.2. Identifying foreground residuals on a single realization

Figure 12 shows the confusion matrix obtained by our training test procedure. The performance of our classifier is as follows (we adopted the convention "clean=negative" and "contaminated=positive"):

- *true negative* rate of very close to 1 indicating that the realizations with no dust residuals (dataset **d1-d1** with $r = 0$ and $r = 0.006$), displayed a constant ratio $\rho(n_{\rm sub})$ and were correctly classified as "clean";
- *true positive* rate very close to 1 indicating that the realizations with dust residuals (dataset **d6-d1** with $r = 0$), displayed a variable ratio $\rho(n_{\rm sub})$ and were correctly classified as "contaminated";
- low *false negative* rate of 2.9% ± 1.6% , indicating a very low percentage of realizations with dust residuals that were wrongly classified as "clean". This is a very important figure of merit that we want to minimize;
- low *false positive* (consistent with 0), indicating a very low percentage of realizations without dust residuals that were wrongly classified as "contaminated".

Such high classification performance demonstrates that BI, with its capability to measure r in several sub-bands, is a promis-

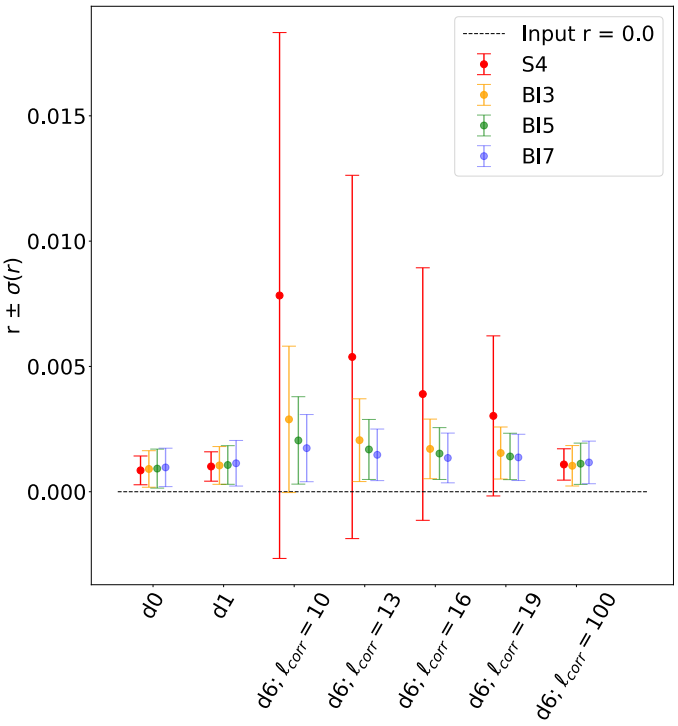

Fig. 11. Summary of the result on r for an input $r = 0$ and all the simulated foreground models (**d0s0**, **d1s1** and several $\ell_{\rm corr}$ cases of **d6s1**).

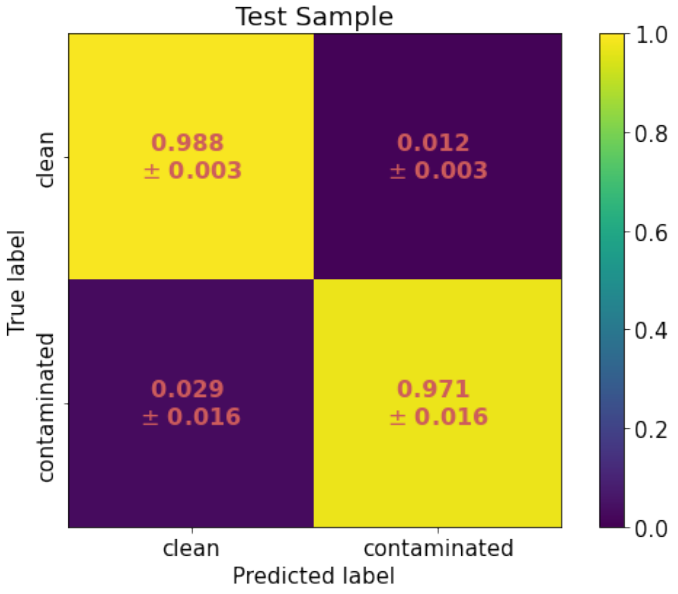

Fig. 12. Confusion matrix representing our ability to classify between our simulated data sets with dust frequency decorrelation (contaminated) or without (clean) using the measurements of r as a function of n_{sub}. We observe that the fraction of false negative ("contaminated" data set incorrectly classified as "clean") is close to zero.

ing solution to identify residuals in the clean CMB maps arising from frequency decorrelation in the dust emission. In such a case, a classical imager lacks the frequency resolution to identify this contamination, leading to a systematic uncertainty in the reconstructed r that is well above the target sensitivity of CMB-S4.

4. Conclusions

In this paper we have shown how bolometric interferometry (BI) has the potential to detect systematic effects caused by interstellar dust in CMB polarization measurements when LOS frequency decorrelation is present in dust emission and it is not accounted for in parametric component separation algorithms.

Although there are ways for imagers to mitigate the problem of not precisely knowing the foreground emission, for example through cross-checking with different component separation methods, such as blind ones (Aumont & Macías-Pérez 2007) or the moment expansion (Chluba et al. 2017; Vacher et al. 2022) which might be less sensitive to foreground mismodeling, in this paper we are proposing a new approach, that is based on a different instrumental configuration, bolometric interferometry, which can be helpful in case of a future B-mode claim to cross-check the result at the instrumental level in addition to other cross-checking at the component separation level.

We have carried out end-to-end simulations with two component separation codes (FGBuster, discussed in the main text, and Commander, discussed in Appendix B), reconstructing the tensor-to-scalar ratio, r, from simulated skies containing CMB, synchrotron and dust emissions, and instrumental noise. For dust emissions we used three models of increasing complexity, one of which contains frequency decorrelation.

We compared two instrument models, CMB-S4 and CMB-S4/BI, the latter being a modified version of CMB-S4 that accounts for the possibility of splitting each physical frequency band in a variable number of sub-bands that can be chosen during data analysis. This feature, which is unique to BI, allows us to assess whether a measurement of r is biased by dust emission residuals or not. Instead, a Fourier-transform spectrometer would suffer from a noise penalty related to not observing all frequencies simultaneously.

Our results are consistent for the two codes and show that with no frequency decorrelation both instruments yield the same performance (the final precision and systematic uncertainty on r is similar). If decorrelation is present and it is not accounted for in component separation then an imager like CMB-S4 would measure a biased value of r. This bias can be reduced with CMB-S4/BI by reanalyzing the same data after splitting the band in increasing number of sub-bands.

This paper is based on a case where the main contamination of CMB, thermal dust, is a more complex than MBB. A model such as an MBB is no longer sufficient to fully describe the contribution of dust and create a bias on the tensor-to-scalar ratio r. In a case like this, we show that BI can improve B-mode sensitivity using a natural method based on software trick.

The decrease of the measured r with the number of sub-bands, $n_{\rm sub}$, clearly indicates the presence of a dust-induced systematic effect, given that without dust residuals the detected r does not change with $n_{\rm sub}$. In a situation like this a classical imager would not have a means to classify the measurement as "clean" or "biased".

We tested the ability to detect biased r measurements also using a machine learning approach, and we verified that assessing the variation of the r measurement versus $n_{\rm sub}$ allowed us to classify clean and biased measurements with a rate > 95%.

Future developments will test this technique in more realistic situations (representative noise, inclusion of optical effects and uncertainty on the knowledge of the instrumental spectral response), assess the performance with various dust models and explore new techniques of component separation, allowing us to separate signals taking into account instrumental effects typical

of bolometric interferometry in a more comprehensive and representative way.

Acknowledgements. QUBIC is funded by the following agencies. France: ANR (Agence Nationale de la Recherche) contract ANR-22-CE31-0016, DIM-ACAV (Domaine d'Intérêt Majeur-Astronomie et Conditions d'Apparition de la Vie), CNRS/IN2P3 (Centre national de la recherche scientifique/Institut national de physique nucléaire et de physique des particules), CNRS/INSU (Centre national de la recherche scientifique/Institut national et al de sciences de l'univers). Italy: CNR/PNRA (Consiglio Nazionale delle Ricerche/Programma Nazionale Ricerche in Antartide) until 2016, INFN (Istituto Nazionale di Fisica Nucleare) since 2017. Argentina: MINCyT (Ministerio de Ciencia, Tecnología e Innovación), CNEA (Comisión Nacional de Energía Atómica), CONICET (Consejo Nacional de Investigaciones Científicas y Técnicas). S. Paradiso acknowledges support from the Government of Canada's New Frontiers in Research Fund, through grant NFRFE-2021-00595. The authors want to thank Alexandre Boucaud for valuable advices about Machine Learning.

References

Abazajian, K., Addison, G. E., Adshead, P., et al. 2022, The Astrophysical Journal, 926, 54
Ade, P., Aguirre, J., Ahmed, Z., et al. 2019, Journal of Cosmology and Astroparticle Physics, 2019, 056
Alonso, D., Sanchez, J., & and, A. S. 2019, Monthly Notices of the Royal Astronomical Society, 484, 4127
Aumont, J. & Macías-Pérez, J. F. 2007, Monthly Notices of the Royal Astronomical Society, 376, 739
Aurlien, R., Remazeilles, M., Belkner, S., et al. 2022, Foreground Separation and Constraints on Primordial Gravitational Waves with the PICO Space Mission
Bigot-Sazy, M.-A., Charlassier, R., Hamilton, J., Kaplan, J., & Zahariade, G. 2013, Astronomy & Astrophysics, 59, 1
Cavaliere, F., Mennella, A., Zannoni, M., et al. 2022, J. Cosmology Astropart. Phys., 2022, 040
Chluba, J., Hill, J. C., & Abitbol, M. H. 2017, Monthly Notices of the Royal Astronomical Society, 472, 1195
Cornwell, T. J. & Wilkinson, P. N. 1981, MNRAS, 196, 1067
D'Alessandro, G., Mele, L., Columbro, F., et al. 2022, Journal of Cosmology and Astroparticle Physics, 2022, 039
D'Alessandro, G., Mele, L., Columbro, F., et al. 2022, J. Cosmology Astropart. Phys., 2022, 039
Eriksen, H. K., Dickinson, C., Lawrence, C. R., et al. 2006, ApJ, 641, 665
Eriksen, H. K., Jewell, J. B., Dickinson, C., et al. 2008, ApJ, 676, 10
Finkbeiner, D. P., Davis, M., & Schlegel, D. J. 1999, The Astrophysical Journal, 524, 867
Hamilton, J. C., Mousset, L., Battistelli, E. S., et al. 2022, J. Cosmology Astropart. Phys., 2022, 034
Hanany, S., Alvarez, M., Artis, E., et al. 2019, PICO: Probe of Inflation and Cosmic Origins
Haslam, C. G. T., Salter, C. J., Stoffel, H., & Wilson, W. E. 1982, A&AS, 47, 1
Hazumi, M., Ade, P., Akiba, Y., et al. 2019, Journal of Low Temperature Physics, 194
Hensley, B. S. & Bull, P. 2018, The Astrophysical Journal, 853, 127
Hensley, B. S. & Draine, B. T. 2017, The Astrophysical Journal, 836, 179
Lewis, A., Challinor, A., & Lasenby, A. 2000, ApJ, 538, 473
Martínez-Solaeche, G., Karakci, A., & Delabrouille, J. 2018, Monthly Notices of the Royal Astronomical Society, 476, 1310
Masi, S., Battistelli, E., de Bernardis, P., et al. 2022, Journal of Cosmology and Astroparticle Physics, 2022, 038
Masi, S., Battistelli, E. S., de Bernardis, P., et al. 2022, J. Cosmology Astropart. Phys., 2022, 038
Masi, S., de Bernardis, P., Columbro, F., et al. 2021, The Astrophysical Journal, 921, 34
McBride, L., Bull, P., & Hensley, B. S. 2023, Monthly Notices of the Royal Astronomical Society, 519, 4370
Mousset, L., Gamboa Lerena, M. M., Battistelli, E. S., et al. 2022, J. Cosmology Astropart. Phys., 2022, 035
O'Sullivan, C., de Petris, M., Amico, G., et al. 2022, J. Cosmology Astropart. Phys., 2022, 041
Pelgrims, V., Clark, S. E., Hensley, B. S., et al. 2021, A&A, 647, A16
Piat, M., Stankowiak, G., Battistelli, E. S., et al. 2022, J. Cosmology Astropart. Phys., 2022, 037
Planck Collaboration, Adam, R., Ade, P. A. R., et al. 2016, A&A, 594, A10
Planck Collaboration, Ade, P. A. R., Aghanim, N., et al. 2014, A&A, 571, A13
Planck Collaboration, Aghanim, N., Ashdown, M., et al. 2017, A&A, 599, A51
Planck Collaboration, Akrami, Y., Ashdown, M., et al. 2020, A&A, 641, A11
Remazeilles, M., Dickinson, C., Banday, A. J., Bigot-Sazy, M. A., & Ghosh, T. 2015, An improved source-subtracted and destriped 408 MHz all-sky map
Ritacco, A., Boulanger, F., Guillet, V., et al. 2023, A&A, 670, A163
Stompor, R., Leach, S., Stivoli, F., & Baccigalupi, C. 2008, Monthly Notices of the Royal Astronomical Society, 392, 216
Thorne, B., Dunkley, J., Alonso, D., & Næss, S. 2017, Monthly Notices of the Royal Astronomical Society, 469, 2821
Torchinsky, S. A., Hamilton, J. C., Piat, M., et al. 2022, J. Cosmology Astropart. Phys., 2022, 036
Vacher, L., Aumont, J., Montier, L., et al. 2022, A&A, 660, A111
Vansyngel, F., Boulanger, F., Ghosh, T., et al. 2018, Astronomy & Astrophysics, 618, C4

Appendix A: Reconstruction of foregrounds parameters

In our paper we focused on the reconstructed tensor-to-scalar ratio, r, as it is the main quantity of interest. The level of systematic uncertainties in the reconstructed r, however, depend on the reconstructed foregrounds spectral parameters and distributions. Thus, in this appendix we focus on foregrouds and discuss the distribution of the foregrounds spectral indices after component separation.

In Fig. A.1 we show the normalized histograms of the difference between the reconstructed and input dust and synchrotron spectral indices, $\Delta\beta_\mathrm{d}$, $\Delta\beta_\mathrm{s}$ for the following three models: **d0s0** (top row), **d1s1** (middle row), **d6s1** (bottom row), all with $r_\mathrm{input} = 0$. Each histogram does not correspond to a particular pixel but contains values from the whole map.

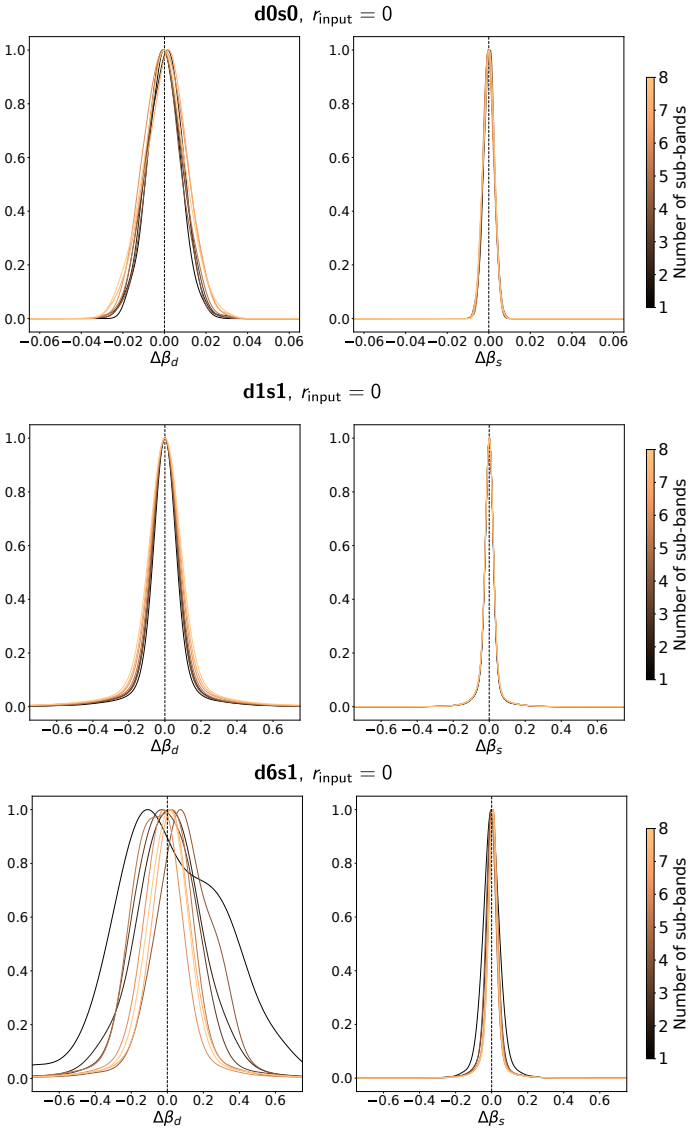

Fig. A.1. Reconstruction of foregrounds spectral indices. *Top*: model **d0s0**, $r_\mathrm{input} = 0$. *Middle*: model **d1s1**, $r_\mathrm{input} = 0$. *Bottom*: model **d6s1**, $r_\mathrm{input} = 0$.

In the case of **d0s0** the model assumes a constant spectral index all over the sky. Therefore we expect unbiased estimates with a standard deviation related to the noise in the input frequency maps. The results shown in the top row of Fig. A.1 confirm this expectation as we observe no bias on the reconstructed spectral indices. We notice that the standard deviation slightly increases with the number of sub-bands, n_sub, because of the slight sub-optimality inherent to spectral-imaging (parametrized by ε in Eq. 4, see Mousset et al. 2022).

When spectral indices vary across the sky, as in **d1s1**, we expect biases in the reconstructed spectral indices because we only reconstruct the spectral indices on relatively large sky pixels ($N_\mathrm{side} = 8$), while the input sky was simulated with spectral indices that vary among smaller pixels ($N_\mathrm{side} = 256$). Consequently, averaging multiple spectral indices in large pixels introduces a bias to the reconstructed spectral index. This bias is responsible for foreground residuals in the CMB maps obtained after component separation and produces the bias on r observed in Fig. 9 and 10.

This is shown in the middle row of Fig. A.1. The bias due to spatial-decorrelation appears as an enlarged spread of the distribution with respect to the **d0s0** case (notice the increased scale of the x-axis in the middle row compared to the top row). Also in this case we observe an increase in standard deviation with n_sub caused by the sub-optimality related to spectral imaging.

Finally, in the case of frequency decorrelation in the dust emission (**d6s1** model) spectral indices are no longer an accurate description of the dust spectral behavior. As a result, if we reconstruct β_d using a **d1s1** model we expect a much larger bias. In this case, the increase in spectral resolution provided by spectral imaging supplies extra information, allowing us to reduce this bias.

This is confirmed by the results shown in the bottom row of Fig. A.1. First, we see a much larger spread in the histograms compared to the other two cases; second, we see that the spread reduces significantly by increasing n_sub. In this case the benefit from spectral imaging more than balances the sub-optimality effect and allows us to reduce the bias on the reconstructed spectral index, correspondingly reducing the bias on r, as shown in Fig. 10.

Appendix B: Simulations with Commander

Appendix B.1: Simulation pipeline

We describe here the simulation pipeline for the analysis performed using the Commander code (Eriksen et al. 2006, 2008). We generated 100 CMB power spectra using CAMB (Lewis et al. 2000) from the set of cosmological parameters shown in Table B.1.

We smoothed both the CMB and foreground signals with a Gaussian beam with FWHM of 1 deg and applied the HEALPix pixel window function at $N_\mathrm{side} = 64$. The only model used to generate the foregrounds is the **d6s1** described in Sect. 3.1.1, in particular setting the dust correlation length to $\ell_\mathrm{corr} = 10$. We considered a 3% sky patch around the center of the one observed by QUBIC. The coordinates of the center of the patch are RA = 0° and DEC = −57°. For computational reasons only four configurations have been studied, namely considering 1, 3, 5 and 7 sub-bands.

For each simulated sky map, we generated a second version of it by taking the same CMB, synchrotron and dust realization, and a different Gaussian noise realization. The analysis chain is the same outlined in Sect. 3.1.3, with the only difference that here we used an apodization radius of 4.6 deg. We performed the component separation sampling the amplitudes $\mathrm{a_{CMB}}, \mathrm{a_s}, \mathrm{a_d}$ and the spectral indices $\beta_\mathrm{s}, \beta_\mathrm{d}$ by means of the following Gibbs

Table B.1. Set of cosmological parameters from the *CAMB Python example notebook* in the CAMB documentation[1].

H_0	67.5
$\Omega_b h^2$	0.022
$\Omega_c h^2$	0.122
Ω_K	0
m_ν	0.06
τ	0.06
$A_s \times 10^{-9}$	2
n_s	0.965

[1] `https://camb.readthedocs.io/en/latest/CAMBdemo.html`

Table B.2. Parameters used for analyzing simulations with Commander.

Number of CMB realizations	100
Map $N_{\rm side}$	64[1]
Multipole range	21–128[2]
$\Delta\ell$	35
Input r	0
Residual lensing fraction	100%[3]
Sky fraction [%]	3%
Sky patch center [Equatorial coord.]	$\alpha = 0°$ $\beta = -57°$
FWHM	1°

[1] Limited by computational time.
[2] Limited by $N_{\rm side} = 64$.
[3] The value of 100% means that all the lensing signal was left.

chain:

$$\{a_{\rm CMB}, a_s, a_d\}^{i+1} \leftarrow P(a_{\rm CMB}, a_s, a_d \,|\, \beta_s^i, \beta_d^i, d) \tag{7a}$$

$$\beta_s^{i+1} \leftarrow P(\beta_s \,|\, a_{\rm CMB}^{i+1}, a_s^{i+1}, a_d^{i+1}, \beta_d^i, d) \tag{7b}$$

$$\beta_d^{i+1} \leftarrow P(\beta_d \,|\, a_{\rm CMB}^{i+1}, a_s^{i+1}, a_d^{i+1}, \beta_s^{i+1}, d)\,. \tag{7c}$$

The spectral indices are sampled at $N_{\rm side} = 8$ as for the FGBuster pipeline. We generated 1000 MCMC samples for each input sky realisation, and discarded the first 100 samples as burn-in. The two noise uncorrelated versions of the same sky realization are associated to two parallel sampling chains. We computed the cross-spectra between these two parallel chains, iteration by iteration, in order to collect a set of 900 spectra for each CMB realization considered in the analysis. We also averaged all of the sampled maps produced in a single chain into a mean map, and for every couple of parallel chains we computed the cross-spectrum between the two mean maps.

After the component separation, we computed the likelihood function for each mean maps' cross-spectrum individually, exploiting the sample-based noise covariance matrix obtained by all the power spectra from the corresponding sampling chain.

Appendix B.2: Results

From the probability distribution of the best fit values obtained with the Commander pipeline, we find that the upper limit to the estimation of a single realization of r is reduced with the number of sub-bands, as shown in Figure B.1. The r bias and $\sigma(r)$ are greater than the FGBuster results due to the marginalization over the foreground components.

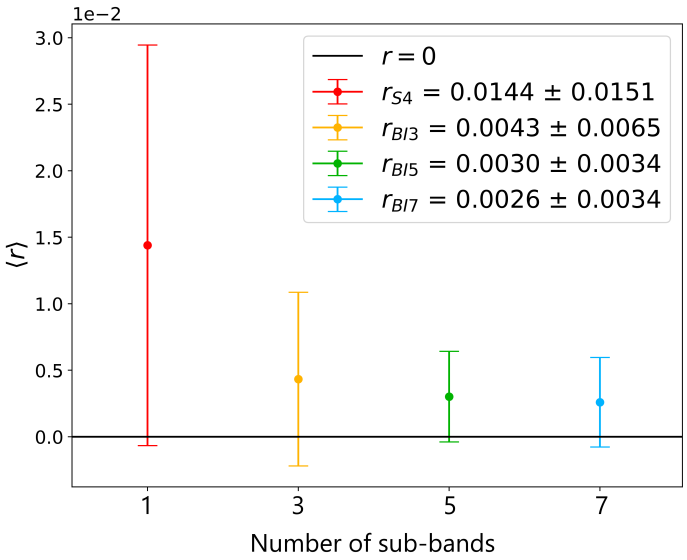

Fig. B.1. Mean and standard deviation of the best fit distributions obtained with the Commander pipeline, using the **d6s1** model with $\ell_{\rm corr} = 10$ and $r = 0$.

Increasing the number of sub-bands also reduces the standard deviation of the spectral indices' marginal distributions for every pixel. Figure B.2 shows the comparison between the reconstructed dust and synchrotron spectral indices for 1, 3 and 5 sub-bands on every pixel. This analysis has not been performed for the 7 sub-bands configuration results because of data storage issues. Here a single $\Delta\beta$ from the plotted distributions represents the difference between the mean value of the marginal distribution on a single pixel for a given sky realization and the template value in the same pixel from the model. These results are in agreement with the FGBuster simulations.

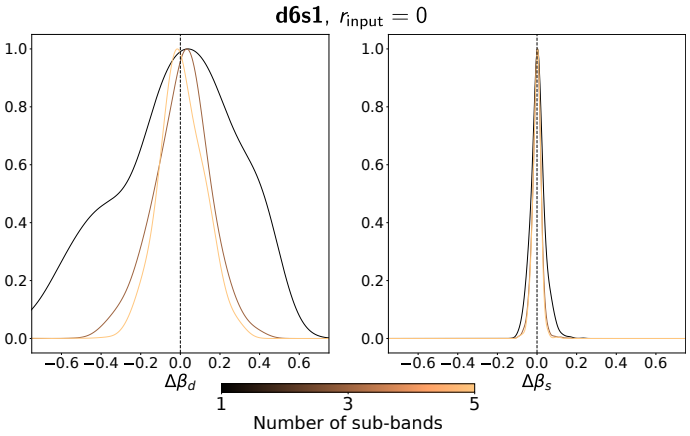

Fig. B.2. : Reconstruction of foreground spectral indices for the **d6s1** model with the Commander pipeline.